## SUPPLEMENTARY FIGURES

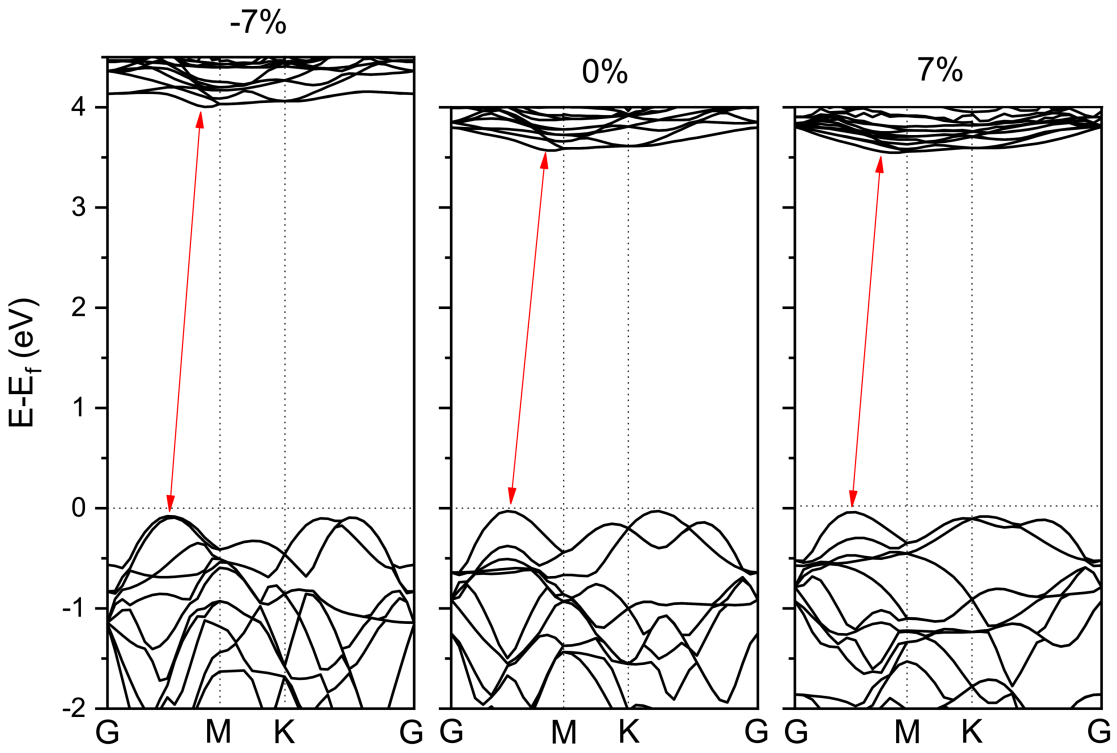


**Supplementary Figure** 1: Band structure in (111)–oriented $CeO_2$ thin films calculated with DFT methods and considering different biaxial strain conditions. The red arrows indicate the top of the valence band and bottom of the conduction band.

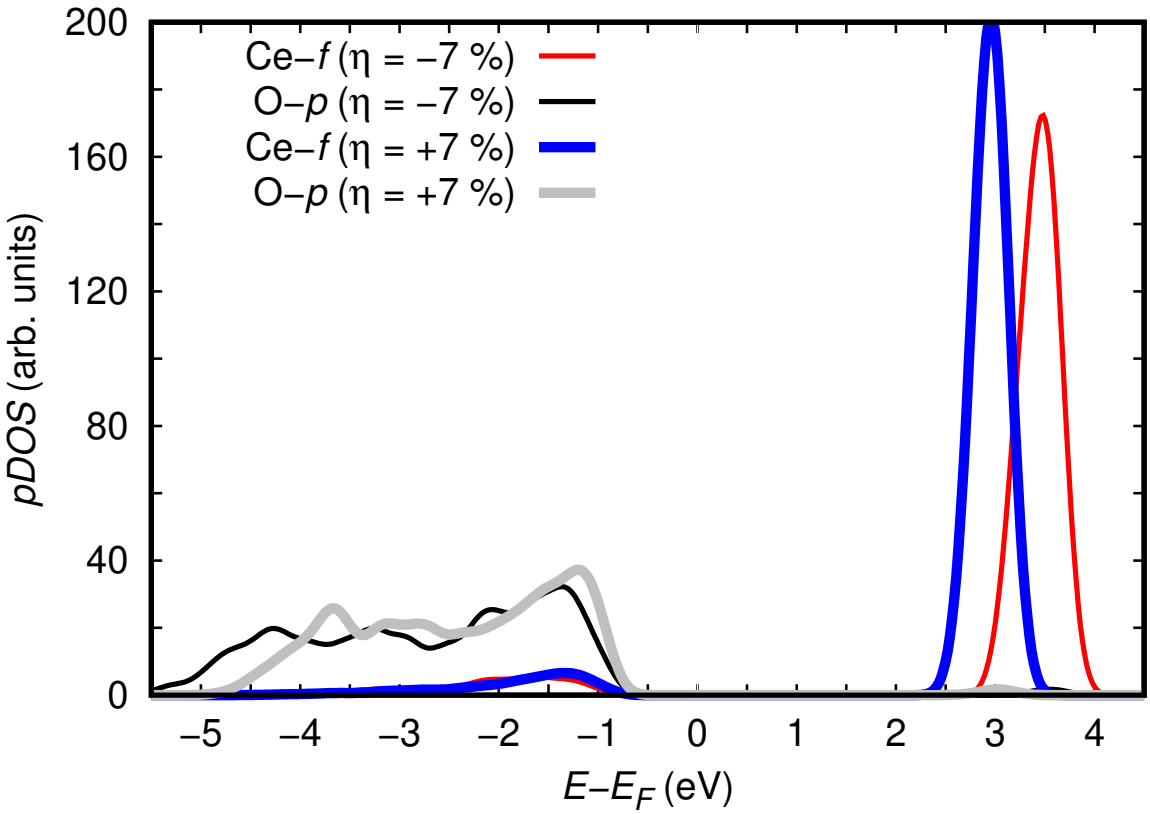


**Supplementary Figure** 2: Partial density of electronic states in (111)–oriented $CeO_2$ thin films calculated with DFT methods and considering different biaxial strain conditions.

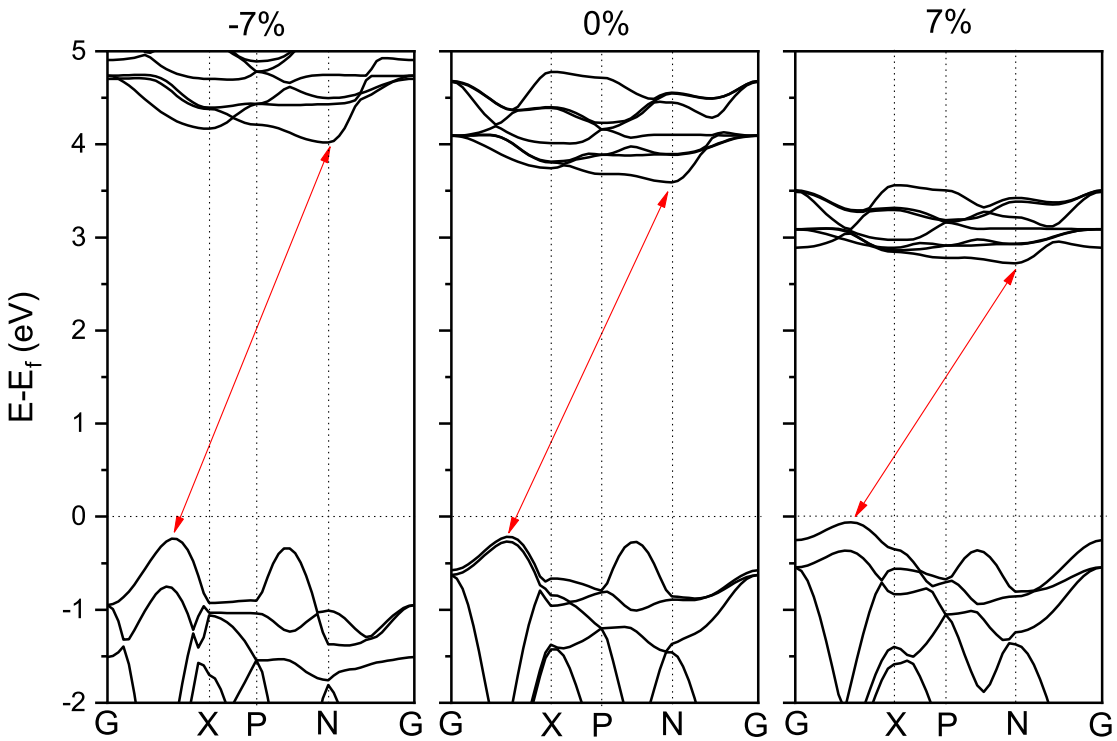


**Supplementary Figure** 3: Band structure in (001)–oriented $CeO_2$ thin films calculated with DFT methods and considering different biaxial strain conditions. The red arrows indicate the top of the valence band and bottom of the conduction band.

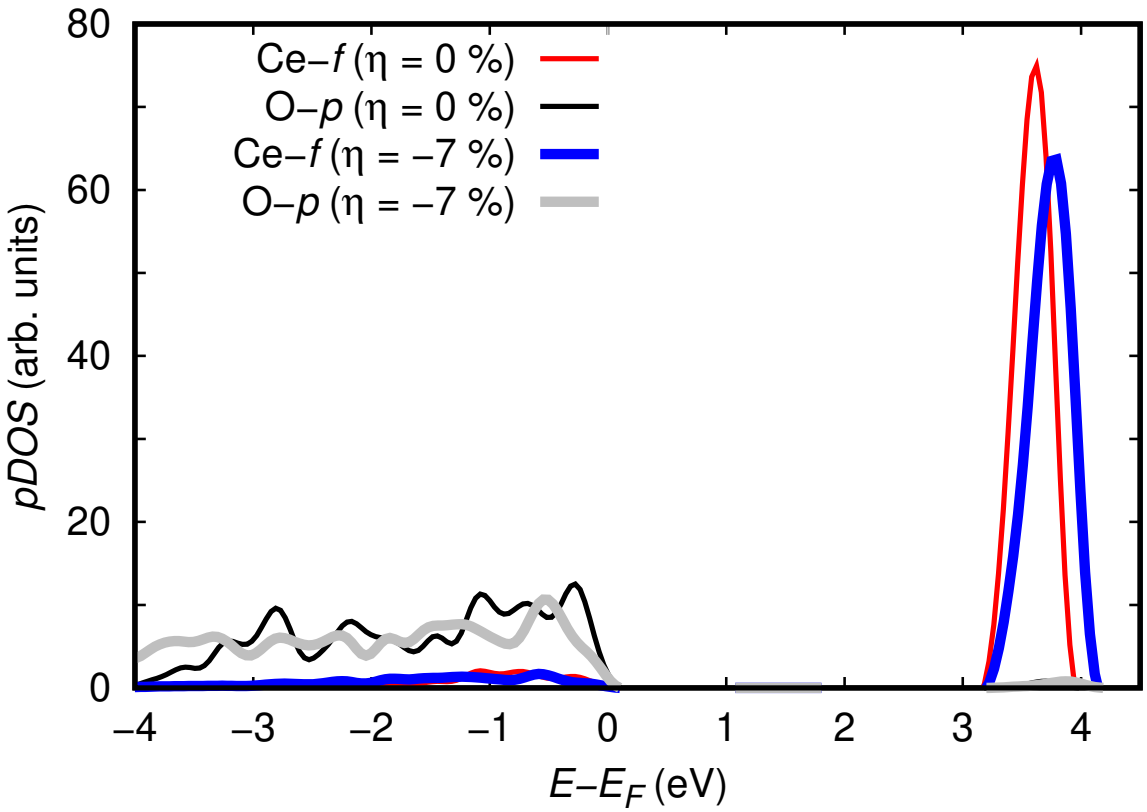


**Supplementary Figure** 4: Partial density of electronic states in (001)–oriented $CeO_2$ thin films calculated with DFT methods and considering different biaxial strain conditions.

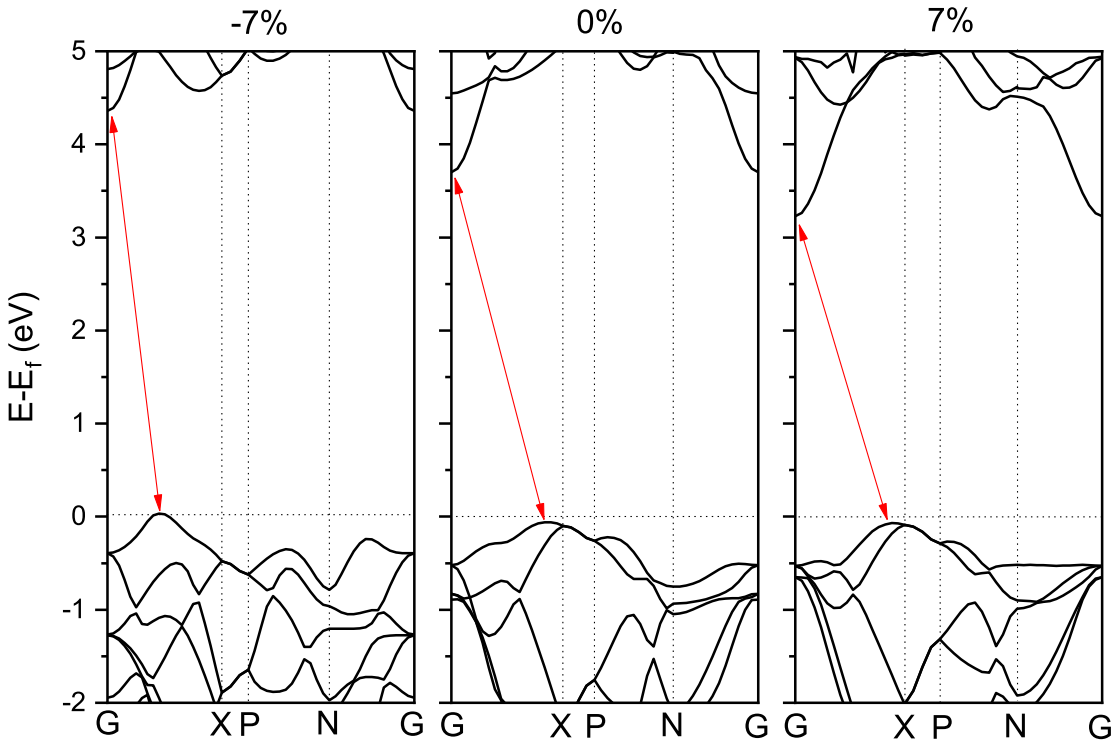


**Supplementary Figure** 5: Band structure in (001)–oriented anatase $TiO_2$ thin films calculated with DFT methods and considering different biaxial strain conditions. The red arrows indicate the top of the valence band and bottom of the conduction band.

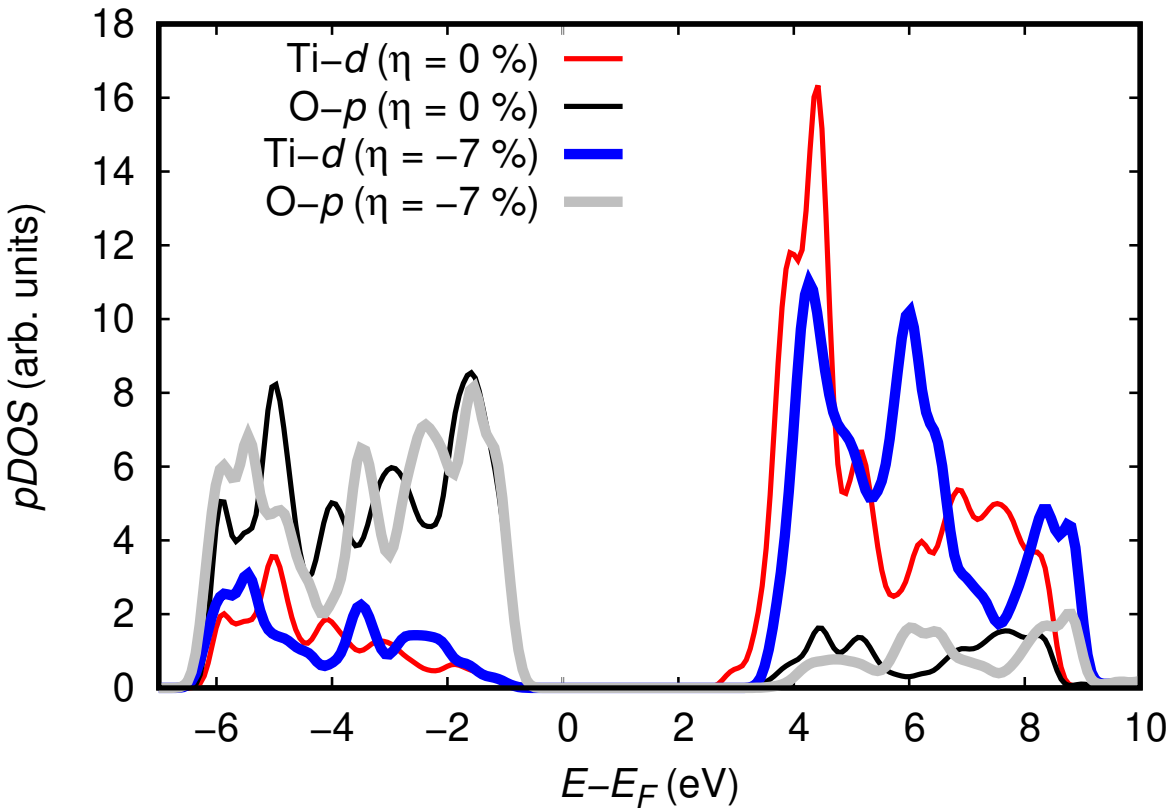


**Supplementary Figure** 6: Partial density of electronic states in (001)–oriented anatase $TiO_2$ thin films calculated with DFT methods and considering different biaxial strain conditions.

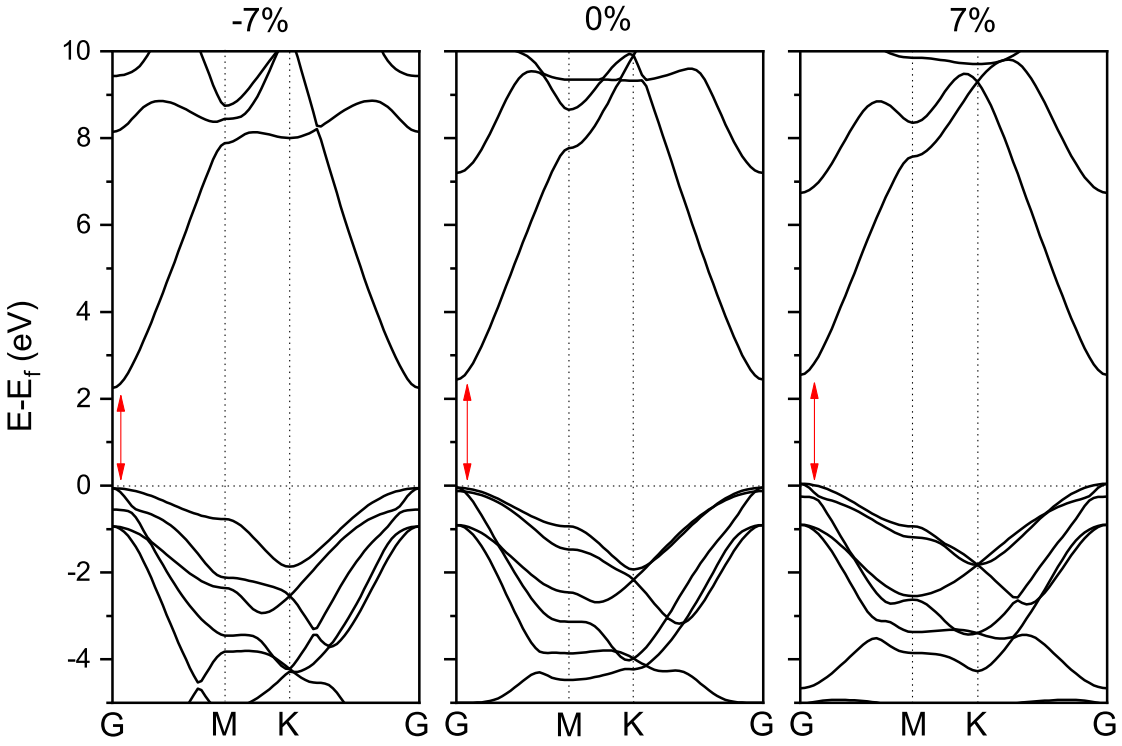


**Supplementary Figure** 7: Band structure in (001)–oriented wurtzite ZnO thin films calculated with DFT methods and considering different biaxial strain conditions. The red arrows indicate the top of the valence band and bottom of the conduction band.

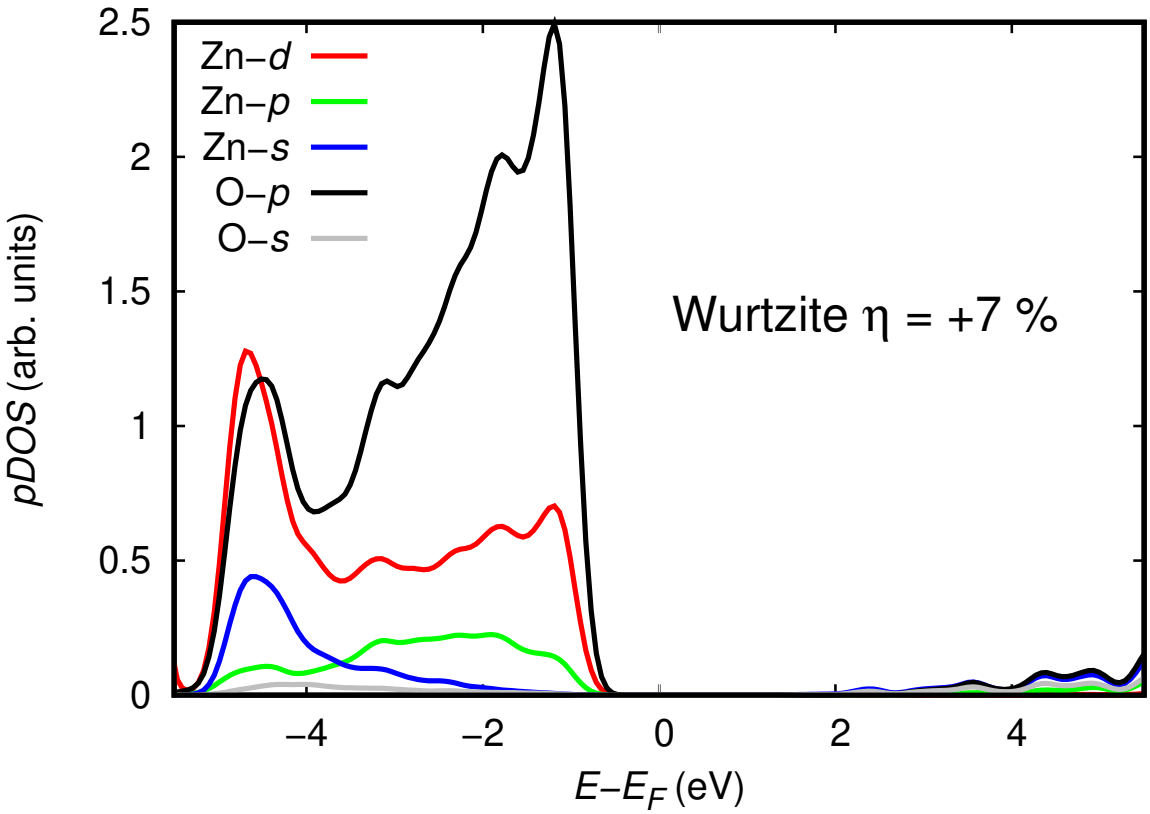


**Supplementary Figure** 8: Partial density of electronic states in (001)–oriented wurtzite ZnO thin films calculated with DFT methods at the maximum tensile strain considered in this study.

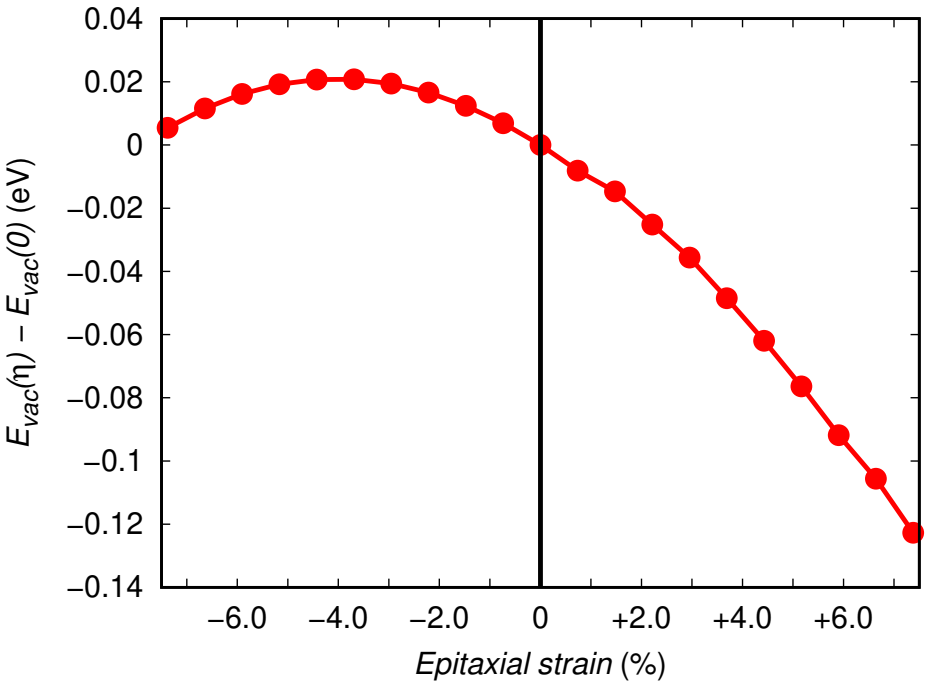


**Supplementary Figure** 9: Oxygen vacancy formation energy in (001)–oriented fluorite $CeO_2$ thin films calculated with DFT methods and expressed as a funcion of biaxial strain conditions. The formation energy is relative to the unstrained case.

## SUPPLEMENTAL METHODS

We performed spin-polarized first-principles calculations based on density functional theory (DFT) to further analyze the changes in atomic and electronic band structure in $CeO_2$ thin films induced by the presence neutral oxygen vacancies ($V_O$) and biaxial strain. We considered a (001)–oriented fluorite $CeO_2$ supercell containing 24 atoms and removed one oxygen atom from it, thus rendering $CeO_{2-\delta}$ with $\delta = 0.125$. Interestingly, the oxygen vacancy formation energy, $E_{vac}(\eta) = E_{Ce_8O_{16}}(\eta) - E_{Ce_8O_{15}}(\eta) - \frac{1}{2}\mu_{O_2}$ (where $E_A$ represents the static energy of system $A$ and $\mu_{O_2}$ the chemical potential of an oxygen molecule), is found to follow a very similar trend to that of the band gap in the corresponding stoichiometric system (Figure 2 in the main text). Specifically, $\Delta E_{vac}$, defined as the energy difference $E_{vac}(\eta) - E_{vac}(0)$, undergoes a significant reduction under tensile strain whereas it remains practically invariant under compressive strain (Supplementary Figure 9). Such a trend similarity hints at a common physical origin of the band gap and $V_O$ formation energy variations observed under biaxial strain.

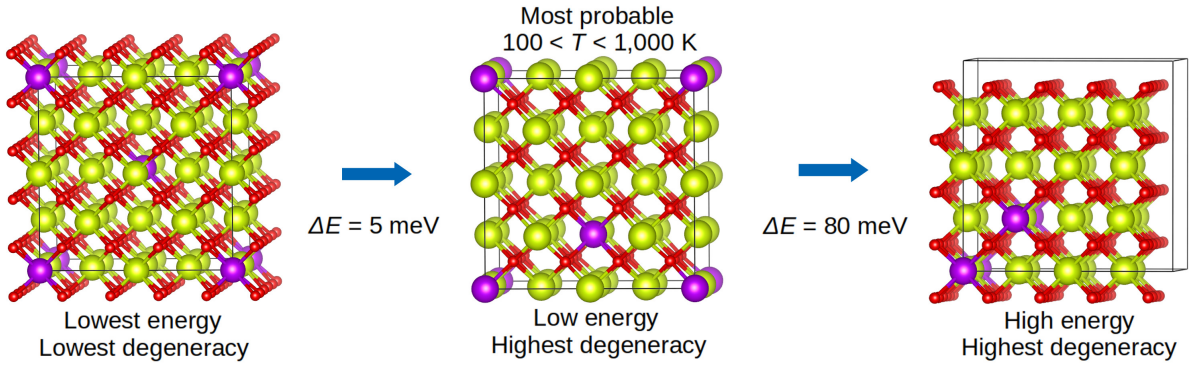


**Supplementary Figure** 10: Energy and configurational analysis of substitutional Gd defects in stoichiometric $CeO_2$. Gd, Ce, and O ions are represented with purple, yellow, and red spheres, respectively. The most probable arrangement of substitutional Gd defects occurring at finite temperatures correspond to the configuration that renders low energy and highest degeneracy.

The effects of biaxial strain on the band gap of Gd-doped $CeO_2$ thin films with (001) orientation were also investigated with DFT methods (Figure 3 in the main text). The parent geometry from which all equilibrium configurations under fixed $\eta$ were obtained, was generated as follows. First, we considered a supercell containing 32 Ce and 64 O atoms. With the help of the SOD software package[1–3], we generated all possible configurations in which two arbitrary Ce ions were substituted by two Gd ions (that is, $Ce_{30}Gd_2O_{64}$); by exploiting the crystal symmetry of the parent fluorite structure, we were able to reduce the huge number of possible combinatorial substitutions to only five inequivalent configurations[1–3]. Upon geometry relaxation of those inequivalent configurations, we were able to determine which arrangement of Ce and Gd ions was thermodynamically most probable to occur in the temperature interval $100 \leq T \leq 1,000$ K, by considering the static energy and configurational entropy of each of them. Irrespective of the temperature, the same configuration emerged always as the most probable (Supplementary Figure 10) thus we selected it to subsequently analyze the preferred position of an oxygen vacancy. Only one oxygen vacancy was considered in our simulations since that is sufficient to preserve charge neutrality in the selected Gd-doped $CeO_2$ system (that is, $Ce_{30}Gd_2O_{63}$). Once again, we considered all possible arrangements of the oxygen vacancy and found that the energetically most favorable site was near one of the two Gd ions (Supplementary Figure 11). Such an arrangement of substitutional Gd atoms and oxygen vacancies was fixed in the subsequent $\eta \neq 0$ simulations

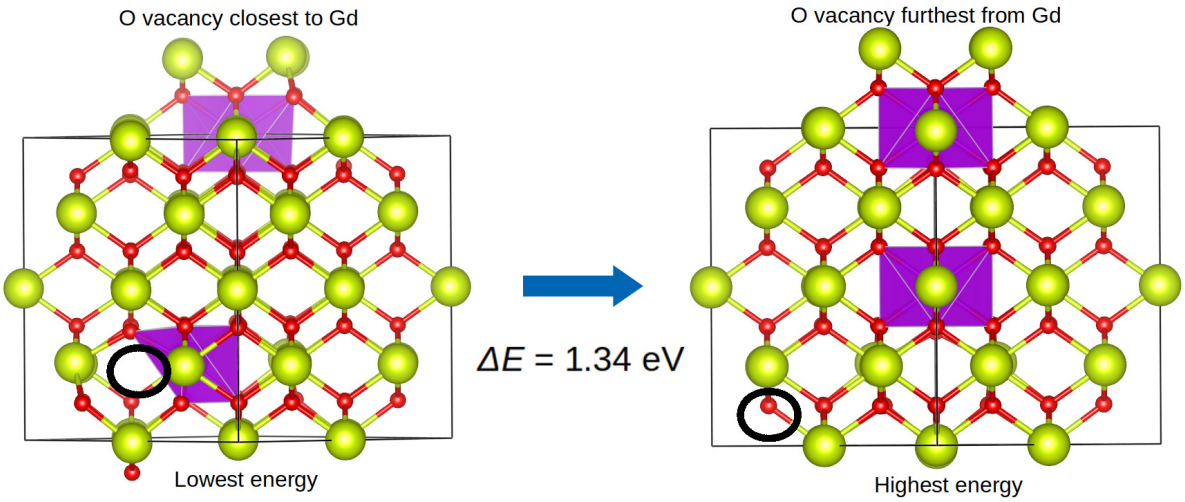


**Supplementary Figure** 11: Energy and structural analysis of $Ce_{1-x}Gd_xO_{2-\delta}$ at low temperatures. Gd, Ce, and O ions are represented with purple, yellow, and red spheres, respectively. The energetically most favorable arrangement for an oxygen vacancy is close to a Gd substitutional defect. Oxygen vacancy positions are indicated with black circles.

performed in (001)–oriented $CeO_2$ thin films.

To calculate accurate band alignments we followed the work by Moses and co-workers done on binary semiconductors[4]. Both bulk and slab calculations were performed to obtain the alignment of the electrostatic potential within the binary oxides relative to the vacuum level. From the slab calculations, we obtained the difference between the macroscopic average electrostatic potential within the semiconductor material and in vacuum (Supplementary Figure 12). The planar potential is computed by averaging potential values within planes that are perpendicular to the surface of the slab, and the macroscopic potential is obtained by taking averages of the planar potential over distances of one unit cell along the same direction[5,6]. A representation of the employed (111) $CeO_2$ and anatase (001) $TiO_2$ slab supercells are shown in Supplementary Figure 12. For anatase (001)–oriented $TiO_2$, we reconstructed the slab surfaces in order to remove its original net dipole moment. In this case, a simulation cell containing a 1.8 nm thick oxide slab and 2.2 nm thick vacuum region was employed. For (111) $CeO_2$, it was not necessary to reconstruct the corresponding slab surfaces and we employed a simulation cell containing a 1.2 nm thick oxide slab and 1.4 nm thick vacuum region. By using these technical parameters, we checked that the electron density in the center of the slab is practically equal to that in the bulk material.

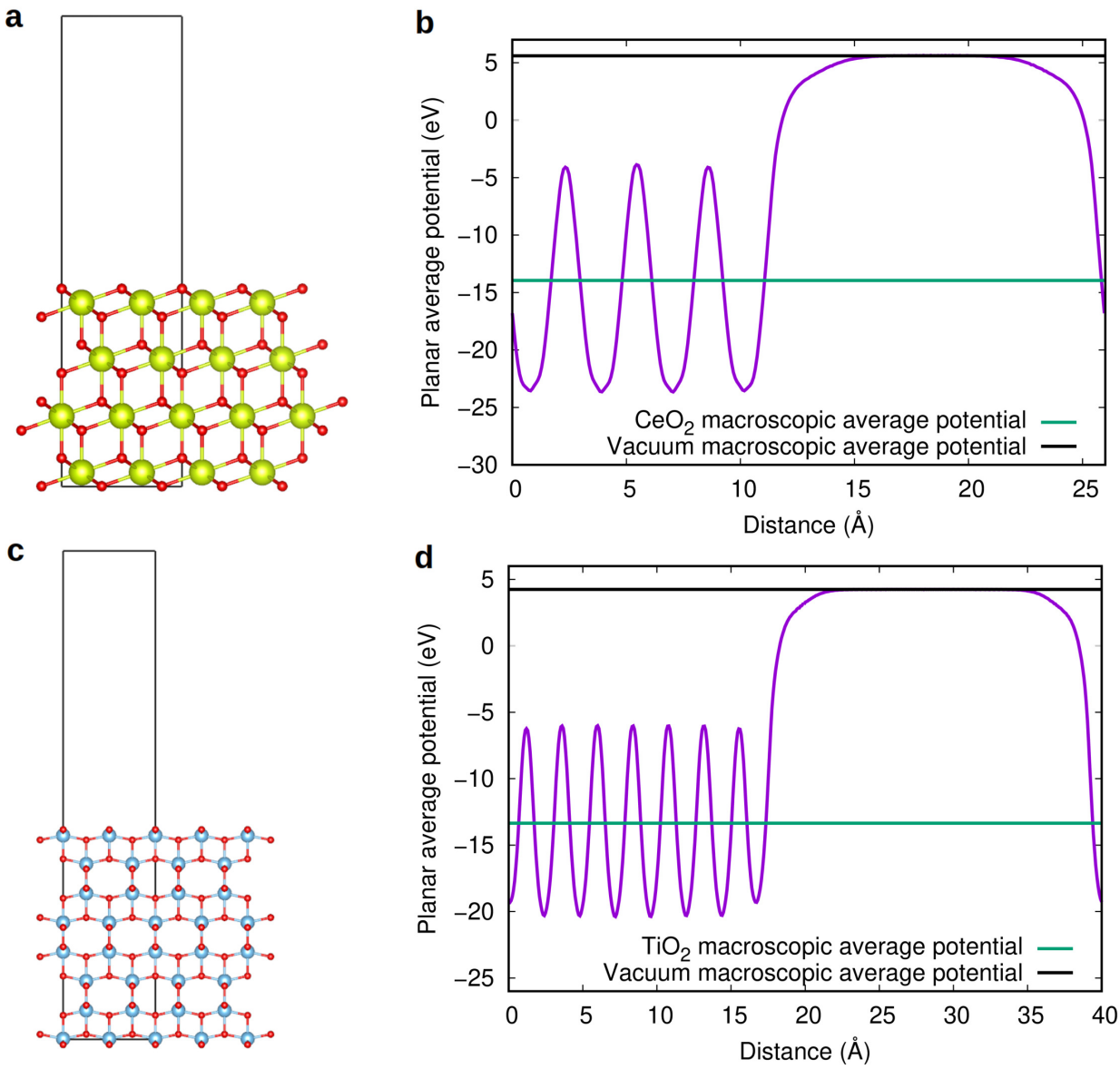


**Supplementary Figure** 12: Technical details of the slab calculations involved in the estimation of band alignments relative to the vacuum level. **a** Representation of the slab simulation cell employed for the band alignment calculations of (111)-oriented $CeO_2$ thin films. **b** Planar (purple line) and macroscopic average (black and green lines) potentials estimated in (111)-oriented $CeO_2$ slabs. **c** Representation of the slab simulation cell employed for the band alignment calculations of anatase (001)-oriented $TiO_2$ thin films. **d** Planar (purple line) and macroscopic average (black and green lines) potentials estimated in anatase (001)-oriented $TiO_2$ slabs.

## SUPPLEMENTARY REFERENCES


[1] Grau-Crespo, R., Hamad, S., Catlow, C. R. A. & de Leeuw, N. H. Symmetry-adapted configurational modelling of fractional site occupancy in solids. *J. Phys. Condens. Matter* **19**, 256201 (2007)

[2] Grau-Crespo, R. & Waghmare, U. V. Simulation of crystals with chemical disorder at lattice sites. *Molecular Modeling for the Design of Novel Performance Chemicals and Materials*, ISBN:1439840784, pp. 299-322, CRC Press (2012).

[3] Shenoy, J., Hart, J. N., Grau-Crespo, R., Allan, N. L. & Cazorla, C. Mixing Thermodynamics and Photocatalytic Properties of GaP-ZnS solid solutions. *Adv. Theory Simul.* **2**, 1800146 (2019).

[4] Moses, P. G., Miao, M., Yan, Q., & Van de Walle, C. G. Hybrid functional investigations of band gaps and band alignments for AlN, GaN, InN, and InGaN. *J. Chem. Phys.* **134**, 084703 (2011).

[5] Baldereschi, A., Baroni, S. & Resta, R. Band offsets in lattice-matched heterojunctions: A model and first-principles calculations for GaAs/AlAs. *Phys. Rev. Lett.* **61**, 734 (1988).

[6] Cazorla, C. & Stengel, M. First-principles modeling of Pt/$LaAlO_3$/$SrTiO_3$ capacitors under an external bias potential. *Phys. Rev. B* **85**, 075426 (2012).